Multiple Reflection Analysis of TDR Signal for Complex Dielectric Spectroscopy

Chih-Ping Lin, Yin Jeh Ngui, and Chun-Hung Lin

***Abstract*— Most dielectric spectroscopy techniques require careful system calibration, tedious measurement, specially designed probes, precise input source, and some even involved complicated inversion models. This paper proposed a rapid, robust, and model-free multiple reflection analysis (MRA) of time-domain reflectometry (TDR) signals to measure the complex dielectric permittivity (CDP) spectrum. The key to MRA approach is to decompose the first top reflection and the subsequent multiple reflections from TDR signal and to compare their spectral ratio (MRA ratio). This ratio was theoretically derived from the transmission line theory and found to be independent of source function and impedance mismatches in the leading sections. Based on this theoretical formulation, the CDP spectrum can be uniquely inverted from the measured MRA ratio through optimization and an iterated initial guess method. Numerical evaluations and experimental verifications had proven that MRA is a reliable algorithm for measuring CDP spectrum covering 10 MHz–1 GHz. Factors influencing the reliable frequency region were discussed and recommendations on enhancing CDP measurement was proposed for highly dispersive materials. The MRA approach enables dielectric spectroscopy to be conveniently conducted in both laboratory and field, without complicated system setup and calibration.**

***Index Terms*— Complex dielectric permittivity (CDP), dielectric spectroscopy, time-domain reflectometry (TDR).**

I. Introduction

DIELECTRIC spectroscopy of materials is of significant importance in revealing the frequency dependence of the materials' electrical properties. Being widely implemented in various scientific and engineering field, dielectric spectroscopy characterizes the polarization, relaxation, and energy dissipation behavior of materials at different frequency range [1]–[4]. In material sciences and biochemical field, substance composition, relaxation behavior, microscopic dynamics, and other polarization properties are studied through their collective dielectric characteristics measured at specific frequencies [5]–[9]. In soil physics, dielectric spectroscopy reveals the macroscopic microwave dielectric behavior of the soil–water mixtures affected by soil type, moisture content, electrical conductivity, and dry density [10]–[14]. Some proposed theoretical models can be verified based on model fitting of the measured dielectric spectrum, in order to assist in characterization and understanding of the measured materials to molecular level [15].

Current practice of dielectric spectrum measurement includes impedance spectroscopy [16]–[22], vector network analyzer [6], [23]–[28], frequency-domain reflectometry [29], [30], and time-domain reflectometry (TDR) [11], [31]–[34]. Amongst the current dielectric spectrum measurement techniques, most of the practices require careful system calibration, tedious sample preparation time, precise input source, and some even involved complicated inversion models. Dielectric spectroscopy in the field is particularly difficult, time-consuming and uneconomical due to complicated system setup and delicate probe design, especially for broadband dielectric spectroscopy at several hundred megahertz.

The research and development of TDR has rapidly progressed over the last several decades, starting from simple cable fault detection up to complex dielectric spectroscopy. Since TDR is capable of measuring dielectric properties over a wide frequency range, TDR has established its foundation as a powerful tool in material science, soil physics [35]–[37], geo-environmental [38], [39], geotechnical [40]–[44], structural [45], and hydrological [46] engineering. Conventional TDR measurement in soil moisture content focuses on the travel time of the time-domain waveform within probe sensing section, in order to gather the singled-valued apparent dielectric constant (K_a). However, rich dielectric information is embedded within the time-domain waveforms and the frequency-dependent dielectric information should be extracted to provide deeper insights into soil composition through dielectric spectroscopy [13], [47], [48]. Lin *et al.* [34] proposed a phase velocity analysis (PVA) approach to measure the apparent dielectric spectrum (ADS) directly from time-domain TDR signals. PVA method extracts the two reflections from the top and end of the sensing probe by proper window selection, calculates their phase shift at each frequency, and determines the corresponding phase velocity spectrum and ADS. The propagation velocity of electromagnetic (EM) waves is frequency dependent and is also a function of the complex dielectric permittivity (CDP). PVA approach is one step closer to creating a simple, model free, and inversion-free CDP measurement technique, except that the measured ADS cannot decouple the real and imaginary parts of CDP

Manuscript received November 28, 2017; revised February 8, 2018; accepted March 12, 2018. This work was supported by the Taiwan's Environmental Protection Administration and Ministry of Science and Technology under Contract MOST 105-2221-E-002-063. The Associate Editor coordinating the review process was Dr. Mohamed Abou-Khousa. *(Corresponding author: Chih-Ping Lin.)*

C.-P. Lin and Y. J. Ngui are with National Chiao Tung University, Hsinchu 30010, Taiwan (e-mail: cplin@mail.nctu.edu.tw).

C.-H. Lin is with National Sun Yat-sen University, Kaohsiung 80424, Taiwan.

Color versions of one or more of the figures in this paper are available online at http://ieeexplore.ieee.org.

Digital Object Identifier 10.1109/TIM.2018.2822404

and expresses them as a joint effect of apparent dielectric permittivity.

Model-based full waveform analysis on TDR waveforms emerged beyond the apparent dielectric permittivity approach for a complete CDP measurement. From earlier layered transmission line framework, Yanuka *et al.* [49] considered multiple reflections but dielectric dispersion is neglected. A measuring system which satisfied the uniform transmission line condition is adapted by Heimovaara [11] and Friel and Or [14], where the dielectric dispersion and conductive loss effect are emphasized. Nonetheless, uniform transmission line system is uncommon in practice, particularly in field measurements, which may be much more complicated. Nonuniform transmission line frameworks are hence proposed by Lin [13] and Feng *et al.* [50] to account for practical scenarios. Both multiple reflections and dielectric dispersion are incorporated in their nonuniform transmission line model, except for the conductor resistance effect. In recent works, a comprehensive TDR waveform modeling approach is presented by Lin and Tang [51]. They developed the forward models based on the input impedance [13] and scatter function S_{11} [50]. The final TDR signal response is determined through a recursive algorithm to reconstruct the full waveform in a bottom-up manner. Nonetheless, separation of the sensing probe and leading sections is difficult due to the recursive algorithm, leading to complicated calibration process and are not yet convenient enough for field implementation.

Various studies in material science and physical chemistry field have successfully measured dielectric spectrum of liquids, which is performed by calculating scatter function from the measured waveform and solving for the corresponding frequency-dependent dielectric permittivity [11], [28], [52], [53]. However, computation of scatter function requires prior information of the system input function and may reduce the robustness of *in situ* application. In order to prevent tedious calibrations of all system sections, several novel techniques were proposed in CDP measurement, for example, triple-short probe calibration [54], short-open-load calibration [55], and two different probe length method [56]. However, specifically designed probes and multiple calibrations were necessary for the aforementioned probes. In light of all these limitations, demand for a simple yet efficient dielectric spectroscopy technique is rising, especially for geo-environmental detection and monitoring industry.

This paper aimed to propose a rapid, robust, and model-free approach for measuring CDP spectrum through time-domain TDR signals. Multiple reflections in TDR signals are usually neglected during signal processing and analysis, which its importance was underestimated. Previous PVA study [34] discovered that by including the multiple reflections of time-domain signals, ADS of some very dispersive materials could still be measured with slight deviation from theoretical value. This paper proposed a multiple reflection analysis (MRA) approach that considers all the multiple reflections from the sensing probe section, and aimed at measuring the CDP spectrum at broader frequency range within 10 MHz–1 GHz. The key to this innovative approach is to decompose the TDR signal into the first top reflection and the remaining all multiple reflections. The ratio of these two parts (MRA ratio) was theoretically derived as a function of the CDP, independent of source function and impedance mismatches. Based on this theoretical formulation, CDP spectrum can be uniquely inverted from the measured MRA ratio. Neither prior information regarding input signal nor dielectric permittivity model is required in the analysis. Having both the simplicity of PVA and the capability of CDP measurement, MRA is computationally efficient and only requires simple system calibration, making it especially suitable for field applications.

Theoretical background of MRA is first established to outline the signal processing and optimization techniques required for CDP spectrum measurement. The proposed MRA approach is next evaluated using numerical simulated and experimentally measured TDR signals in eight selected materials [distilled water (DIS), tap water (TAP), acetone (ACE), air (AIR), methanol (MTH), ethanol (ETH), isopropanol (IPA), and butanol (BUT)], covering both nondispersive and dispersive materials from high to low dielectric permittivity.

II. Theoretical Development

A. Multiple Reflections in a TDR Signal

A typical TDR measurement system is comprised of a step pulse generator, oscilloscope, transmission cable, and a sensing probe. A step pulse is emitted by the pulse generator into the leading cable until the sensing probe, where the EM wave is exposed to the measured material along the probe sensing section. All occurring incidents and reflections within the TDR system were recorded by the oscilloscope. In an open-ended matched probe system, the first two main reflections arise from the interfaces at probe-head—sensing section, and probe-end—open-circuit, due to discontinuous characteristic impedance. Multiple reflections after the first two main reflections exist as the remaining portion of transmitted signal energy continues to propagate and reflect back and forth within the probe, until the remaining energy dies out and the response reaches a steady state. To describe the multiple reflections of TDR signals, some fundamentals of transmission line system modeling is first established.

Transmission line theory is adopted in system modeling as the dominant mode of TDR system is essentially the 1-D transverse EM mode [50]. As EM wave propagates through the transmission line, decay and phase changes of the wave in phasor form are described by a propagation function H

$$H(x, \varepsilon^*(f)) = \exp[-2\gamma(f)x] \tag{1}$$

where x is the traveling distance, f is the frequency, and γ is the frequency-dependent propagation constant and defined as

$$\gamma(f) = \alpha + j\beta = \frac{j2\pi f}{c}\sqrt{\varepsilon^*(f)} \tag{2}$$

where α and β are the real and imaginary parts of the propagation constant, describing the attenuation and phase changes of waves, respectively, j is $\sqrt{-1}$, c is the speed of light, while $\varepsilon^*(f)$ is the frequency-dependent CDP defined by

$$\varepsilon^*(f) = \varepsilon'(f) + j\varepsilon''(f) \tag{3}$$

where ε' and ε'' are the real and imaginary parts of CDP, respectively.

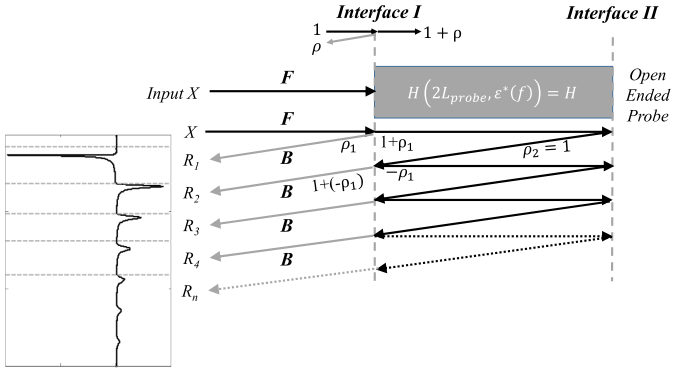

Fig. 1. Ray tracing diagram for all TDR reflections.

Reflections and transmissions occurring at impedance mismatched interface between section i and $i+1$ can be described using the reflection coefficient ρ_i and transmission coefficient τ_i

$$\rho_i = \frac{Z_{c,i+1} - Z_{c,i}}{Z_{c,i+1} + Z_{c,i}} \tag{4}$$

$$\tau_i = 1 + \rho_i \tag{5}$$

where Z_c is the characteristic impedance and defined as

$$Z_c = \frac{Z_p}{\sqrt{\varepsilon^*(f)}} \tag{6}$$

in which Z_p is the geometric impedance (i.e., characteristic impedance in AIR).

Fig. 1 illustrates the ray tracing diagram of an input X propagating along the cable and partial of the forward wave is reflected back from interface I. The first main reflection pulse (hereinafter referred to as R_1) is denoted by [34]

$$R_1 = X \cdot F \cdot \rho_1 \cdot B \tag{7}$$

in which F and B are the forward and backward propagation functions in the leading transmission line, while ρ_1 is the reflection coefficient at interface I. The remaining signal is transmitted into the probe sensing section proportionally according to the transmission coefficient τ_1.

During the signal transmission within the sensing section, the surrounding material influences the propagating wave and its effect is characterized by $H(x, \varepsilon^*(f))$. Upon reaching interface II at the open end, ρ_2 is equal to 1 according to (4) and all transmitted signal is reflected back at this interface. The reflected wave passes back through sensing section, while the coefficient of both reflection and transmission occurring at interface I are $-\rho_1$ and $1-\rho_1$, respectively. Ray path of the second main reflection pulse (hereinafter referred to as R_2) described above is hence

$$\begin{aligned} R_2 &= X \cdot F \cdot (1+\rho_1) \cdot H(2L, \varepsilon^*(f)) \cdot (1-\rho_1) \cdot B \\ &= X \cdot F \cdot B \cdot H(2L, \varepsilon^*(f)) \cdot (1-\rho_1^2) \end{aligned} \tag{8}$$

where L is the probe length and $x = 2L$ since the wave propagated back and forth within the probe. For formulation simplicity, the system function of probe sensing region $H(2L, \varepsilon^*(f))$ is denoted as H hereinafter.

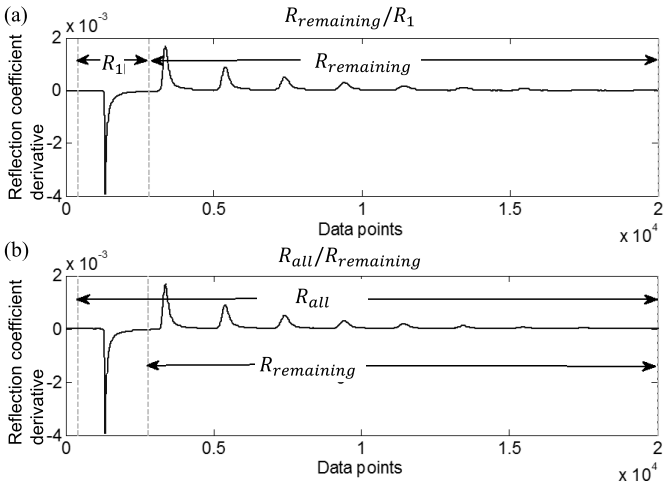

Fig. 2. MRA. (a) Approach 1. (b) Approach 2.

Multiple reflections following the similar path of R_2 above but with weaker input signal of reflected R_2 will result in $R_3, R_4, \ldots, R_n$, each gets weaker and eventually dies out. Following the ray path and formulation above, the multiple reflections can be expressed as

$$\begin{aligned} R_3 &= \frac{R_2}{1-\rho_1} \cdot (-\rho_1) \cdot H \cdot (1-\rho_1) \\ &= X \cdot F \cdot B \cdot H \cdot \left(1-\rho_1^2\right) \cdot H \cdot (-\rho_1) \end{aligned} \tag{9}$$

$$\begin{aligned} R_4 &= \frac{R_3}{1-\rho_1} \cdot (-\rho_1) \cdot H \cdot (1-\rho_1) \\ &= X \cdot F \cdot B \cdot H \cdot \left(1-\rho_1^2\right) \cdot H^2 \cdot \rho_1^2 \end{aligned} \tag{10}$$

Observing the pattern of odd and even numbered multiple reflections, the consecutive multiple reflections can be expressed in a general form as

$$R_k = XFBH(1-\rho_1^2)[H(-\rho_1)]^{(k-2)} \tag{11}$$

for $k = 2, 3, 4, 5, 6, \ldots$. For equations within this section, X, F, and B are system parameters and not the targets being measured.

B. Multiple Reflection Analysis (MRA)

The CDP $\varepsilon^*(f)$ of interests lies within both $H(x, \varepsilon^*(f))$ and ρ_1. Taking the spectral ratio of some extracted reflection signals, the system functions X, F, B are canceled out and the ratio becomes purely a function of H and ρ_1, independent of input function and leading transmission line sections. The desired $\varepsilon^*(f)$ information can be extracted from H and ρ_1 for nontrivial conditions. Two MRA approaches with different spectral ratio combination are first proposed, while their sensitivity and performance in CDP spectrum measurement are discussed next.

MRA approach 1 (MRA1) takes the spectral ratio of the remaining reflections after the first main reflection (hereinafter referred to as $R_{\text{remaining}}$, i.e., $R_2 + R_3 + R_4 + \cdots$) to the first main reflection R_1, as shown in Fig. 2(a). Following the

general form of multiple reflections in (11), $R_{\text{remaining}}$ can be derived as

$$R_{\text{remaining}} = \sum_{k=2}^{\infty} R_k = X \cdot F \cdot B \cdot H \cdot (1-\rho_1^2) \cdot \sum_{k=2}^{\infty} [H \cdot (-\rho_1)]^{(k-2)} \quad (12)$$

Replacing $k = n + 2$, the last term is a geometric series summation which can be computed as

$$\sum_{n=0}^{\infty} [H \cdot (-\rho_1)]^n = \frac{1}{1-(-\rho_1 H)} \quad (13)$$

where $|-\rho_1 H| < 1$ must be satisfied for the above equation to be valid. Combining (12) and (13), $R_{\text{remaining}}$ is now

$$R_{\text{remaining}} = X \cdot F \cdot B \cdot H \cdot \left(1-\rho_1^2\right) \cdot \frac{1}{1+\rho_1 H}. \quad (14)$$

Recalling R_1 from (7), the spectral ratio of MRA1 is hence

$$\text{MRA1} = \frac{R_{\text{remaining}}}{R_1} = \frac{H \cdot (1-\rho_1^2)}{\rho_1 \cdot (1+\rho_1 H)} \quad (15)$$

where two assumptions of $|-\rho_1 H| < 1$ and $\rho_1 \neq 0$ must be satisfied for MRA1 to be valid and nontrivial.

MRA approach 2 (MRA2) is the spectral ratio of all reflections starting from probe head (hereinafter referred to as R_{all}, i.e., $R_1 + R_2 + R_3 + R_4 + \cdots$) to $R_{\text{remaining}}$, as shown in Fig. 2(b). Since R_{all} is equal to the summation of R_1 and $R_{\text{remaining}}$, R_{all} is obtained by summing up (7) and (14)

$$\begin{aligned} R_{\text{all}} &= R_1 + R_{\text{remaining}} \\ R_{\text{all}} &= [X \cdot F \cdot B \cdot \rho_1] + \left[X \cdot F \cdot B \cdot H \cdot \left(1-\rho_1^2\right) \cdot \frac{1}{1+\rho_1 H}\right] \\ &= X \cdot F \cdot B \cdot \left[\frac{\rho_1 + H}{1+\rho_1 H}\right] \end{aligned} \quad (16)$$

Comparing (14) and (16), the ratio of MRA 2 is now

$$\text{MRA2} = \frac{R_{\text{all}}}{R_{\text{remaining}}} = \frac{(\rho_1 + H)}{H \cdot \left(1-\rho_1^2\right)} \quad (17)$$

where the assumption of $|-\rho_1 H| < 1$ also must be satisfied because of (13).

Two main differences between the two approaches are: 1) the value contrast of MRA2 is significantly larger than MRA1 at higher frequencies and 2) improper signal processing technique may lead to signal truncation of R_1 in MRA1. Signal leakage from R_1 into $R_{\text{remaining}}$ is still a potential issue for both approaches and its effect is investigated numerically in further section. Implementation of appropriate signal processing in MRA1 could effectively reduce R_1 truncation effect. This paper evaluated the CDP measurement integrity of the proposed method mainly with MRA1, while using MRA2 as supplementary ratio to perform CDP crosschecking.

C. Signal Processing

MRA CDP measurement is performed by fitting the theoretical MRA, a function of $\varepsilon^*(f)$ in (15) or (17), to the measured MRA ratio (MRA_{mea}) at each frequency without a dielectric dispersion model. Four inputs are required for the MRA approach, namely, Z_{ch}/Z_{p1}, L, $R_{\text{remaining}}$ and either

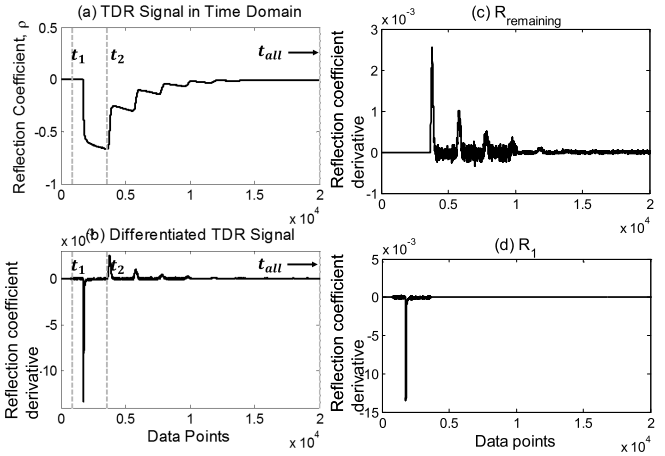

Fig. 3. MRA signal processing illustration (using water as example). (a) TDR step signal. (b) Differentiated TDR impulse signal. (c) Extracted $R_{\text{remaining}}$. (d) Extracted R_1.

R_1 (MRA1) or R_{all} (MRA2). The first two inputs are the system parameters that are required to be calibrated prior to fitting optimization, namely, the probe length (L) and the ratio of probe head and probe sensing section (Z_{ch}/Z_{p1}). The probe length is required for the traveling distance x of $H(x, \varepsilon^*(f))$ in (1), and can be measured directly from the probe. The Z_{ch}/Z_{p1} ratio is required for determining ρ_1

$$\rho_1 = \frac{Z_{c1} - Z_{\text{ch}}}{Z_{c1} + Z_{\text{ch}}} = \frac{1 - \frac{Z_{\text{ch}}}{Z_{c1}}}{1 + \frac{Z_{\text{ch}}}{Z_{c1}}} = \frac{1 - \frac{Z_{\text{ch}}}{Z_{p1}}\sqrt{\varepsilon_1^*}}{1 + \frac{Z_{\text{ch}}}{Z_{p1}}\sqrt{\varepsilon_1^*}} \quad (18)$$

where Z_{ch} and Z_{c1} are the characteristic impedances of probe head and probe sensing section, respectively, Z_{p1} is the geometric impedance of the probe sensing section. For a probe with regular geometric cross section, both Z_{ch} and Z_{p1} can be calculated from EM theory. For arbitrary geometric cross sections, Z_{ch}/Z_{p1} can be measured through a calibration using material of known CDP.

The remaining MRA inputs required signal processing technique to extract them from TDR signals. $R_{\text{remaining}}$ is extracted from the probe end onward and is defined at t_2 in Fig. 3(b). t_2 is suggested to be the lowest reflection coefficient of step pulse signal in Fig. 3(a) and it usually passes through zero in the derivative signal. For MRA1, R_1 is suggested to be close to the probe head, denoted as t_1 in Fig. 3(a) and (b), but for a matched probe head system, there is no difference since the TDR signal before probe head is flat. For MRA2, R_{all} is the complete recorded TDR signal beginning from probe head, preferably until the steady state of the multiple reflections and typically approximately 2×10^{-7} s signal recording time, depending on material under testing (MUT) dielectric properties and sensing probe length.

A typical TDR waveform measured by a matched probe in water is shown in Fig. 3(a) to illustrate the MRA measurement procedures. TDR step pulse signal is first differentiated into impulse signal of Fig. 3(b) and next decomposed into two parts in MRA. Tukey window [57] is applied to the extracted impulses to regulate the tranquil state at two ends, before

TABLE I
COLE–COLE PARAMETERS OF SELECTED MUTS FOR TDR WAVEFORM SIMULATION

MUT	Abbreviation	ε_{dc}	ε_{∞}	f_{rel} (GHz)	σ_{dc} ($\mu S/cm$)	β
Distilled water [14]	DIS	80.20	4.22	17.4	0	0.0125
Tap Water [14]	TAP	78.54	4.22	17	300	0.0125
Acetone [30]	ACE	21.20	1.90	47.65	0	0
Air	AIR	1.00	1.00	-	0	0
Methanol [30]	MTH	33.64	5.70	3.002	0	0
Ethanol [61]	ETH	25.50	4.25	0.782	0	0
Isopropanol [6]	IPA	19.34	2.48	0.448	0	0
Butanol [13]	BUT	17.70	3.30	0.274	0	0

performing fast Fourier Transform [58] on the time-domain signals. MRA spectral ratios are computed in frequency domain according to (15) or (17), in order to obtain $\mathrm{MRA_{mea}}$. Frequency range (f_{opt}) of 10 MHz–1 GHz is chosen for CDP optimization as this is the typical effective frequency range for TDR signals.

An arbitrary yet reasonable initial guess $\varepsilon^*_{\mathrm{ini}}$ comprising of both real and imaginary parts of CDP is selected for MRA fitting optimization. Theoretical system functions H and ρ_1, and theoretical MRA ratio ($\mathrm{MRA_{theo}}$) are computed based on the opted initial guess, starting from the lowest frequency in f_{opt}. $\mathrm{MRA_{theo}}$ is next optimized with regard to $\mathrm{MRA_{mea}}$ until the minimum cost is found for the cost function of CDP ($\mathrm{CF_{MRA}}$), which is the root-mean-square error between $\mathrm{MRA_{theo}}$ and $\mathrm{MRA_{mea}}$. This optimization process is iterated by every frequency steps within f_{opt} until the complete CDP spectrum of the MUT is generated.

III. NUMERICAL EVALUATION ON MRA METHOD

A. Generation of Synthetic TDR Signals

The proposed MRA is first numerically evaluated using synthetic TDR data. System parameters selected in the waveform simulation is similar to experimental setup for direct comparison between numerically simulated and experimentally measured data. A three-section transmission line model was hence selected, comprising of a 42-m 50-Ω coaxial cable, a 0.1-m 50-Ω matched probe head and a 0.17-m coaxial probe sensing section with $Z_p = 95\Omega$.

Eight MUTs with different dielectric dispersion and electrical conductivity characteristics were simulated, namely, DIS, TAP, ACE, AIR, MTH, ETH, IPA, and BUT. A comprehensive wave propagation model established by Lin and Tang [51] was implemented in theoretical TDR signal simulation. Cole–Cole function [59] is selected as the dielectric relaxation model in this paper to describe the dielectric behaviors of MUT, which describes $\varepsilon^*(f)$ by

$$\varepsilon*(f) = \varepsilon_{\infty} + \frac{\varepsilon_{\mathrm{dc}} - \varepsilon_{\infty}}{1 + (jf/f_{\mathrm{rel}})^{1-\beta}} - \left(\frac{j\sigma}{2\pi f \varepsilon_0}\right) \tag{19}$$

where ε_{∞} and $\varepsilon_{\mathrm{dc}}$ are the dielectric constants at frequencies of infinite and static condition, respectively, f_{rel} is the relaxation frequency, and $\beta$is the symmetrical shape parameter of dielectric loss spectrum. This dielectric model assumes that the dielectric loss peak of MUT is of symmetrical broadening. Cole–Cole function parameters of MUT are tabulated in Table I and MUT is abbreviated for simplicity. Both system functions H and ρ_1 are dependent on the $\varepsilon^*(f)$ characterized above. CDP of both the transmission cable and probe head are assumed as $1 + 0i$ throughout the dielectric spectrum, while a mild cable resistance effect is considered by assuming cable resistance loss factor, $\alpha_r = 50$ in signal simulation.

As aforementioned, two system parameters are required for MRA computation, which is the probe length (L) and the impedance ratio of probe head to sensing section (Z_{ch}/Z_{p1}). Probe length is directly measured from the actual probe and taken as 0.17 m in the numerical simulation. The latter system parameter, Z_{ch}/Z_{p1} is determined by direct measurement of the coaxial probe, using the characteristic impedance determination equation [60] in the following:

$$Z_c = \frac{1}{2\pi}\sqrt{\frac{\mu_0}{\varepsilon_0 \cdot \varepsilon_r}} \ln \frac{D}{d} \tag{20}$$

where μ_0 is the vacuum permeability, D is the inner diameter of external conductor, and d is the outer diameter of internal conductor. For this paper, Z_{ch} and Z_{p1} of the matched coaxial probe are found (set) to be 50 and 97 Ω, respectively, Z_{ch}/Z_{p1} is thus 0.5155.

TDR signals were simulated with 5-ps sampling time and the total simulation time window was 1.3107×10^{-7} s. For presentation clarity, the simulated time-domain signals shown in Fig. 4 was truncated from approximately 1 m before sensing section and the truncated time window duration was 2×10^{-7} s, which was found to be sufficient for the signals to reach their steady state. The first four MUTs in Table I are less dispersive and are shown in Fig. 4(a), while the last four dispersive alcohol type MUTs are shown in Fig. 4(b). Fig. 4(c) shows a zoomed-in TDR waveforms of the alcohols for better visual.

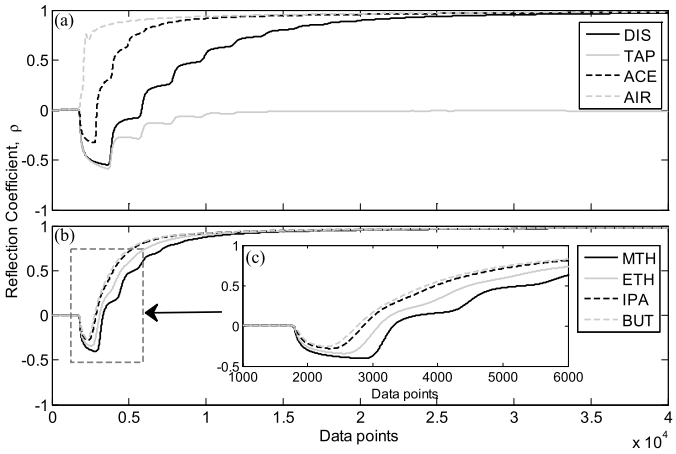

Fig. 4. Simulated TDR waveforms for MUTs in Table I. (a) Less dispersive MUTs. (b) Dispersive alcohol type MUTs. (c) Zoomed-in waveforms of (b).

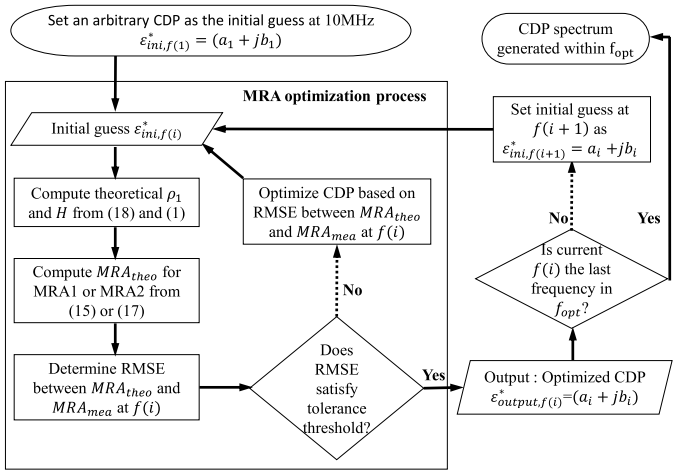

Fig. 6. Flowchart of iterated initial guess implementation in MRA.

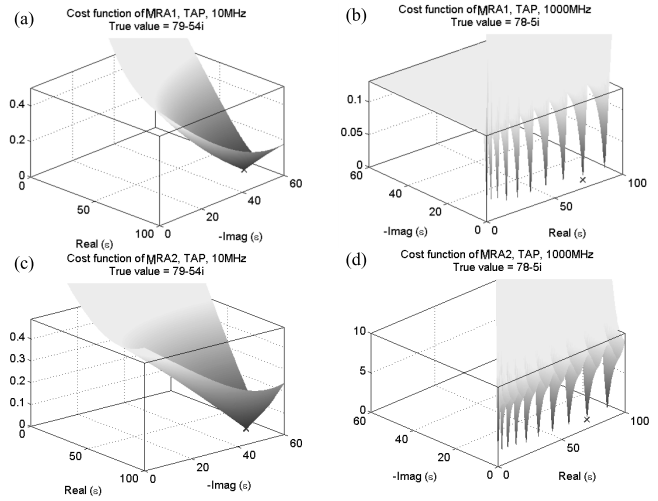

Fig. 5. Theoretical MRA ratio cost function structure. (a) MRA1 at 10 MHz. (b) MRA1 at 1 GHz. (c) MRA2 at 10 MHz. (d) MRA2 at 1 GHz.

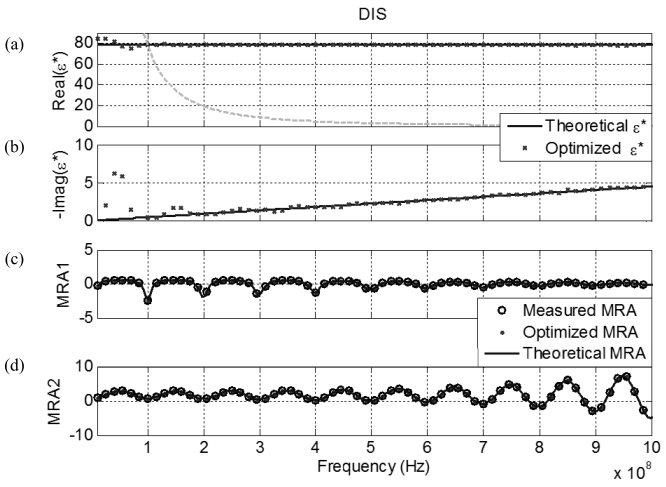

Fig. 7. MRA1 on simulated DIS. (a) Real $\varepsilon^*(f)$. (b) -Imaginary $\varepsilon^*(f)$. (c) MRA1 ratio. (d) MRA2 ratio.

B. Optimization Function and Initial Guess Selection

All simulated TDR signals were processed according to the aforementioned MRA procedure and analyzed by both approaches to compare their performances, using a commercial software package MATLAB [62]. Optimization function adopted in this paper is the readily available fminsearch function, which uses the Nelder–Mead simplex direct search algorithm to find the minimum of unconstrained multivariable function using derivative-free method. Initial guess inputted to the optimization cost function is one of the key issues for optimization problems. Local minimums often exist in some cost function structures. If the initial guess deviates from the true value too much, the optimization path may fall into the nearby local minimum and may result in erratic outcome. In order to investigate the consistency and stability of optimization process in MRA, we investigated the cost function structure for both MRA approaches in both real (ε^*) and imaginary (ε^*) domains. Using the aforementioned system setup, MRA_{theo} is computed for TAP to demonstrate the cost function structure at 10 MHz and 1 GHz.

Fig. 5 illustrates the cost function structure of the theoretical MRA ratio obtained from (15) and (17) for MRA1 and MRA2, respectively. It is observed that for both approaches, there are no local minimums at 10 MHz and only a global minimum exists for MRA1 and MRA2 at 10 MHz, as shown in Fig. 5(a) and (c). However, as the frequency increases up to 1 GHz, the number of local minimums increases accordingly and this is the aforementioned undesirable scenario for optimization problems. Nevertheless, the absence of local minimums at lower frequencies is a favorable circumstance, so we propose an iterated initial guess method based on this phenomenon to solve initial-guess-dependent optimization problem. Since there is a good cost function structure at lower frequencies, an arbitrary $\varepsilon^*_{\text{ini},f(i)}$ (with both real and imaginary parts) is given as the initial guess at the lowest f_{opt} and through the MRA optimization routine, a correctly optimized $\varepsilon^*_{\text{output},f(i)}$ is obtained. This $\varepsilon^*_{\text{output},f(i)}$ is then set as the initial guess $\varepsilon^*_{\text{ini},f(i+1)}$ for MRA optimization at the next frequency step. A detailed flowchart illustrating the iterated initial guess implementation in MRA optimization is

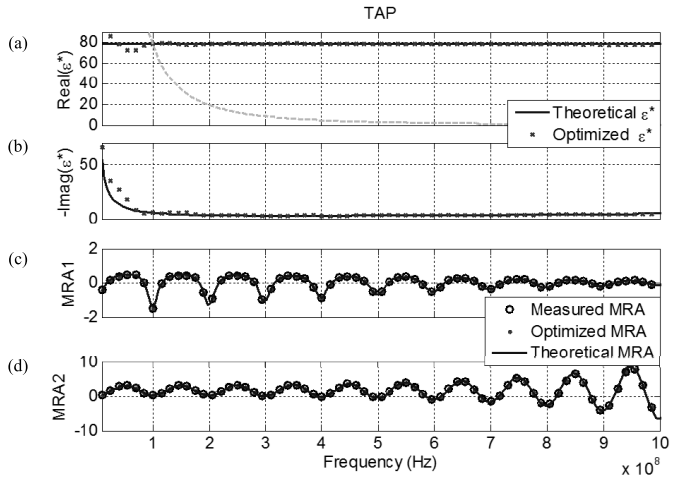

Fig. 8. MRA1 on simulated TAP. (a) Real $\varepsilon^*(f)$. (b) -Imaginary $\varepsilon^*(f)$. (c) MRA1 ratio. (d) MRA2 ratio.

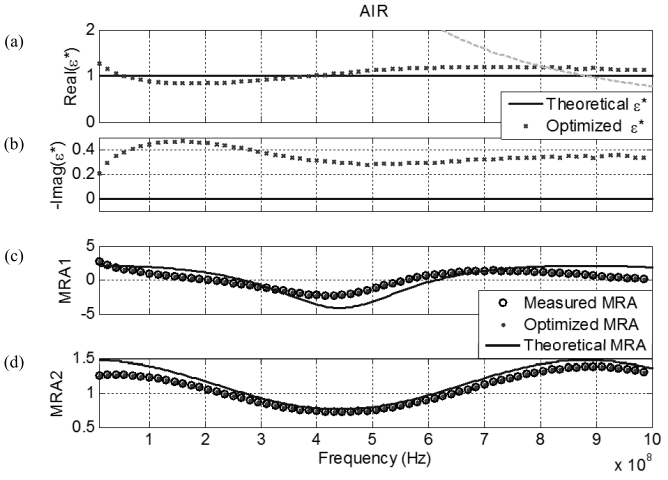

Fig. 10. MRA1 on simulated AIR. (a) Real $\varepsilon^*(f)$. (b) -Imaginary $\varepsilon^*(f)$. (c) MRA1 ratio. (d) MRA2 ratio.

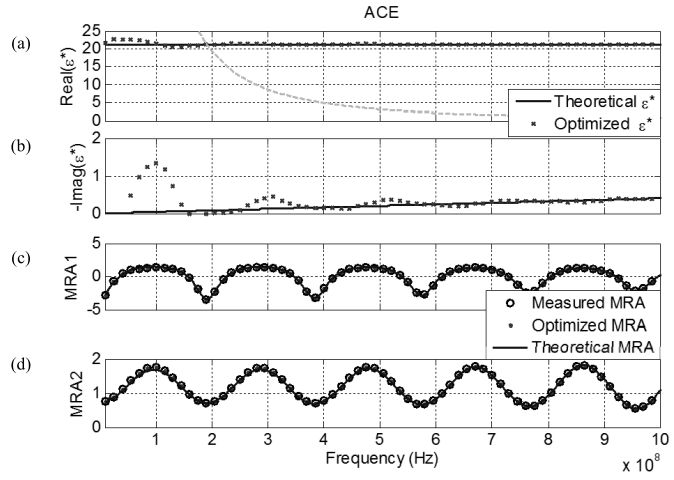

Fig. 9. MRA1 on simulated ACE. (a) Real $\varepsilon^*(f)$. (b) -Imaginary $\varepsilon^*(f)$. (c) MRA1 ratio. (d) MRA2 ratio.

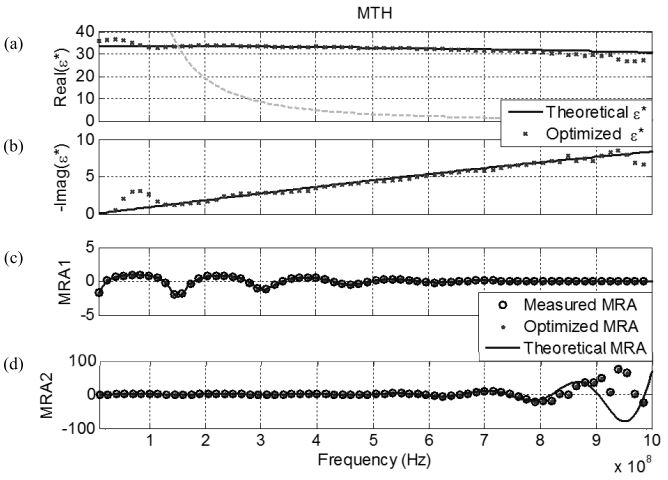

Fig. 11. MRA1 on simulated MTH. (a) Real $\varepsilon^*(f)$. (b) -Imaginary $\varepsilon^*(f)$. (c) MRA1 ratio. (d) MRA2 ratio.

shown in Fig. 6. This iterated initial guess method eliminates the need for global optimization and provides a relatively initial-guess-independent optimization environment for MRA approach. An arbitrary yet reasonable initial guess of CDP of $\varepsilon^*_{\text{ini},f(1)} = 10 + i$ was assigned to the optimization function of all MUTs.

C. Performance of MRA Method on Synthetic Signals

Figs. 7–14 show the CDP spectrum of each MUT generated by MRA1. Subplots (a) and (b) are the real and imaginary parts of optimized CDP, respectively, which match their theoretical values (marked as solid lines) very well within certain frequency range. Frequency interval (df) during MRA optimization was set as 5 MHz and the frequency interval shown CDP spectrum plots were downsampled to 15 MHz for presentation clarity.

Slight oscillations may be observed in the CDP spectrum due to the presence of noise induced by the input signal. It can be seen that beyond certain lower frequency limit, the oscillations become more apparent and induces more CDP deviation. This is caused by leakage of R_1 into $R_{\text{remaining}}$, which its effect would be more severe in case of higher cable resistance effect. A quick demonstration using DIS is shown in Fig. 15, where two different cable resistance cases of α_r of 0 (nonresistive) and 50 (resistive) were simulated for the 42-m preceding cable. As seen from Fig. 15(b) and (c), beyond a certain lower frequency limit [marked as faint dotted lines in subplot (b)], optimized CDP from nonresistive cable case shows no significant deviation from theoretical value. Signal leakage phenomenon induced by resistive cable is observed in $\alpha_r = 50$ case and caused a higher oscillated optimized CDP beyond a frequency limit. A shorter cable or a high quality cable is therefore recommended to minimize cable resistance impact.

In case of inevitable cable resistance scenario, potential affected frequency range maybe estimated by delineation of a lower frequency limit. The lower frequency limit is physically dependent on the probe length, which is reflected in the

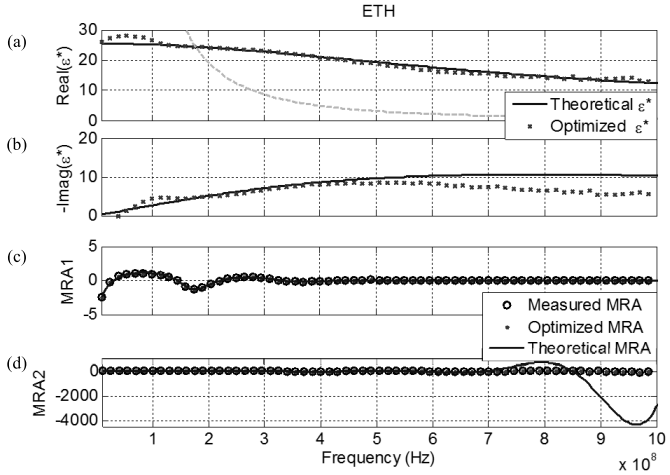

Fig. 12. MRA1 on simulated ETH. (a) Real $\varepsilon^*(f)$. (b) -Imaginary $\varepsilon^*(f)$. (c) MRA1 ratio. (d) MRA2 ratio.

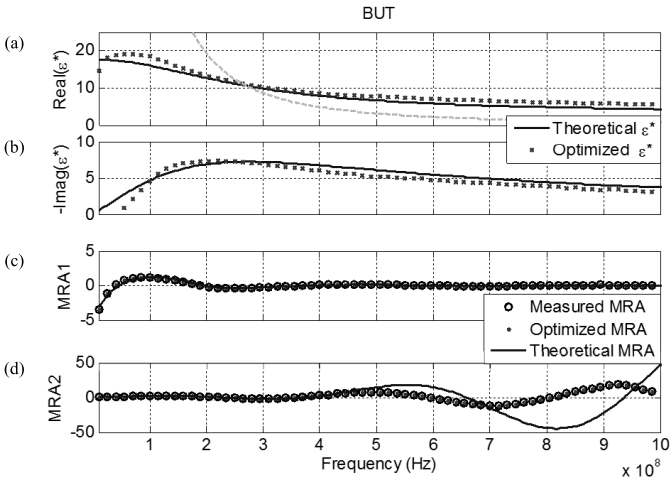

Fig. 14. MRA1 on simulated BUT. (a) Real $\varepsilon^*(f)$. (b) -Imaginary $\varepsilon^*(f)$. (c) MRA1 ratio. (d) MRA2 ratio.

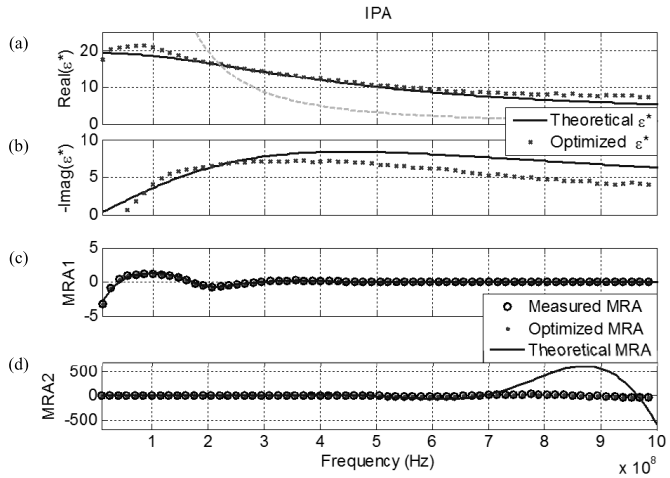

Fig. 13. MRA1 on simulated IPA. (a) Real $\varepsilon^*(f)$. (b) -Imaginary $\varepsilon^*(f)$. (c) MRA1 ratio. (d) MRA2 ratio.

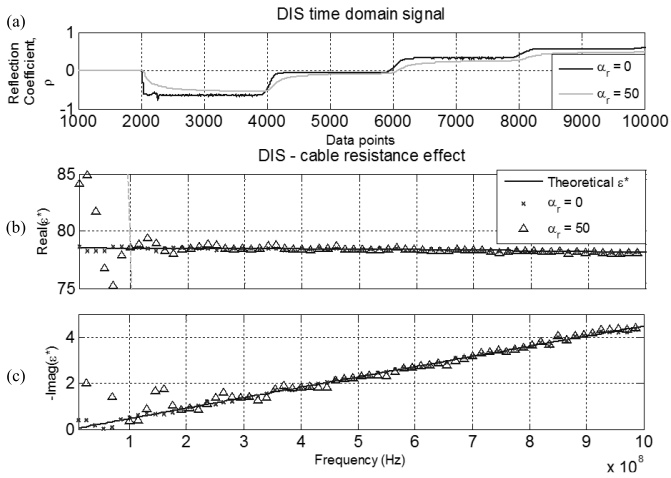

Fig. 15. Cable resistance effect in MRA, demonstrated using DIS. (a) Time-domain signals of DIS. (b) Real $\varepsilon^*(f)$. (c) -Imaginary $\varepsilon^*(f)$.

length of the truncated R_1. Since recorded TDR signal is a combination of forward and backward propagating waves, the maximum workable wavelength ($\lambda_{\text{workable}}$) is about two times the sensing probe length. The lower frequency limit of CDP spectrum f_{lower}, can be approximated from the physical probe length by

$$\lambda_{\text{workable}} = 2 \times L_{\text{probe}} \tag{21}$$

$$f_{\text{lower}} = \frac{V_{\text{MRA}}}{\lambda_{\text{workable}}} = \frac{c}{2L_{\text{probe}}\sqrt{\varepsilon'}} \tag{22}$$

where L_{probe} is the sensing probe length and c is the speed of light. Note that this lower frequency limit is particularly useful for TDR signals with higher cable resistance effect, in identifying possible frequencies affected by signal leakage when measuring unknown MUT. A dashed line is marked in subplots (a) of Figs. 7–14 to provide an estimation of reliable lower frequency boundary.

Throughout the measured CDP spectrums of the eight MUTs, the application of iterated initial guess in MRA is indeed a good solution to reduce the dependence of initial-guess-dependent optimization. In subplot (c) of the eight MUTs, the optimized MRA1 (denoted as "∗") is shown to fit accurately to the measured MRA1 (denoted as "o"), indicating that there were no optimization issues with local minimum. MRA2 ratio in subplot (d) is plotted for crosschecking and to assess MRA performance at higher frequencies. It can be observed that MRA1 ratios for all MUTs have lower values at higher frequencies, which is inevitable due to the presence of the term $(1 - \rho_1^2)$ in the numerator of (15). At higher frequencies, the term approaches zero and leads to lower MRA1 ratio, which is very close to zero. This may lead to lower CDP sensitivity, especially during optimization process where numerical optimization usually relies on gradient search and eventually falls into local minimums. However, due to the implementation of iterated initial guess, accuracy of CDP measured via both MRA1 and MRA2 are satisfactory.

CDP spectrums of the four nondispersive MUTs (DIS, TAP, ACE, and AIR) were measured correctly above the lower frequency limit. As their dielectric permittivity is nondispersive across the measured TDR spectrum, leading to a

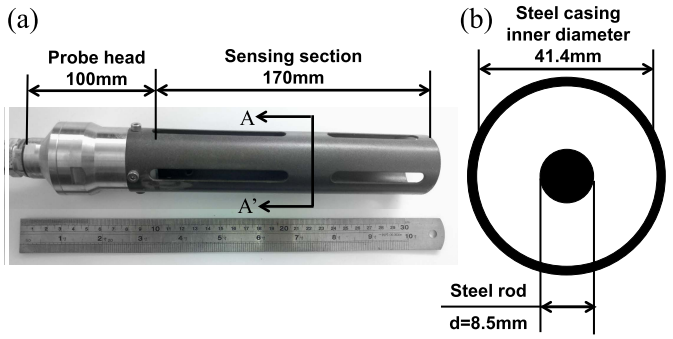

Fig. 16. (a) TDR matched coaxial field probe. (b) Cross section of A–A′ in (a).

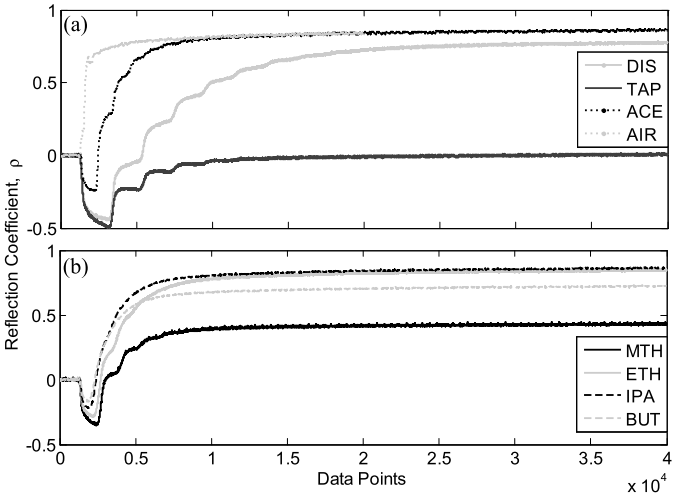

Fig. 17. Experimental TDR waveforms. (a) Less dispersive MUT. (b) Dispersive alcohol type MUT.

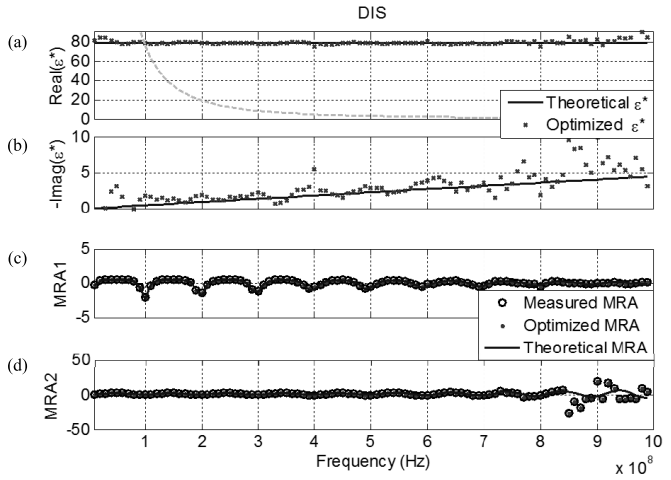

Fig. 18. MRA1 on DIS. (a) Real $\varepsilon^*(f)$. (b) -Imaginary $\varepsilon^*(f)$. (c) MRA1 ratio. (d) MRA2 ratio.

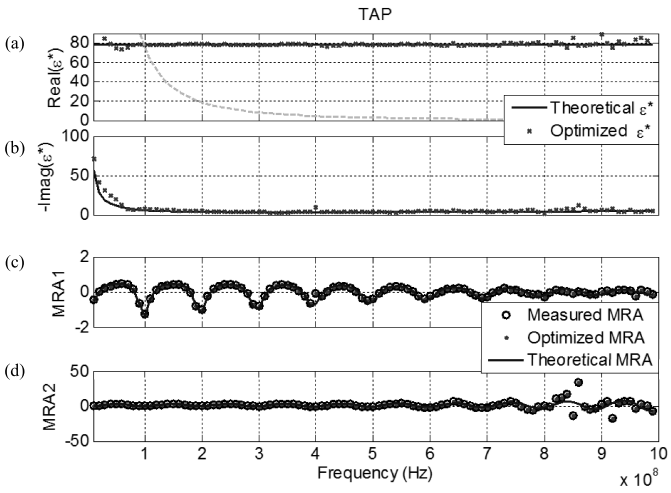

Fig. 19. MRA1 on TAP. (a) Real $\varepsilon^*(f)$. (b) -Imaginary $\varepsilon^*(f)$. (c) MRA1 ratio. (d) MRA2 ratio.

sharper waveform and lowering effect from possible signal truncation or leakage. Close inspection on the CDP spectrums of alcohol type MUTs (MTH, ETH, IPA, and BUT) revealed that there were some deviation in higher frequencies, especially for ETH and IPA with higher dielectric loss. Dielectric dispersion is significant for these dispersive MUTs and their dispersive, flatter signals tend to leak from R_1 into $R_{\text{remaining}}$. Signal leakage effect of dispersive alcohol affected MRA as the deviation in higher frequencies. For alcohol type MUTs with high dielectric dispersion, their MRA2 ratio typically have a large value contrast at high frequencies, in which some increased drastically up to several order of magnitude as the dispersion loss effect comes in. The apparent deviation between theoretical and measured MRA2 ratio is convenient in identifying frequency region with signal leakage influence.

Reliability of the proposed MRA approach is proven numerically. The proposed method is capable of measuring both real and imaginary parts of CDP spectrum with simple system calibration on the probe length (L) and the impedance ratio of probe head and probe sensing section (Z_{ch}/Z_{p1}), without any prior information regarding input signal or transmission line sections before the probe head. Both MRA1 and MRA2 approaches are complementary in CDP spectrum integrity delineation. MRA approach performs well with the assistance of iterated initial guess method and avoids potential local minimums during optimization. Further validation on MRA is performed by measuring CDP spectrum from experimental waveforms.

IV. Experimental Validation on MRA Method

A. Measurement System

Eight MUTs adopted in the experimental validation is the same as previous MUTs selected for numerical evaluation. The laboratorial measurement system consisted of a broadband TDR device with 3.35-GHz bandwidth, a 50-Ω coaxial cable, a modularized 0.1-m 50-Ω matched stainless steel probe head and a 0.17-m coaxial probe sensing section of $Z_p = 95\Omega$. Time-domain signals were obtained by generating a step EM pulse with a short rise time (10%–90%) of 95 ps into the matched stainless steel probe, via the 42-m coaxial cable and N to BNC connectors. All eight TDR signals were measured

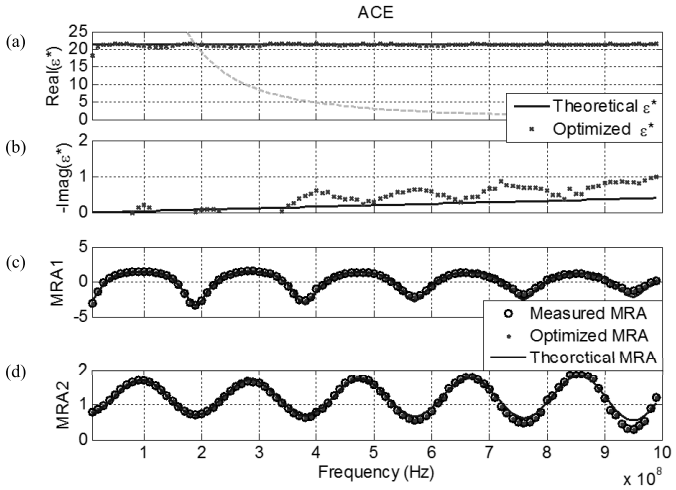

Fig. 20. MRA1 on ACE. (a) Real $\varepsilon^*(f)$. (b) -Imaginary $\varepsilon^*(f)$. (c) MRA1 ratio. (d) MRA2 ratio.

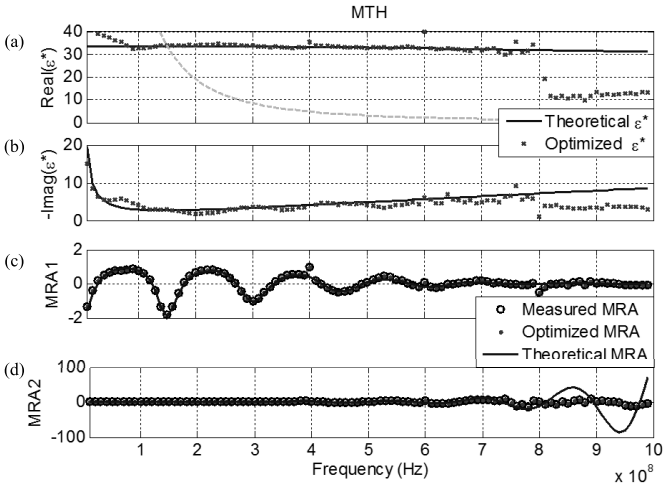

Fig. 22. MRA1 on MTH. (a) Real $\varepsilon^*(f)$. (b) -Imaginary $\varepsilon^*(f)$. (c) MRA1 ratio. (d) MRA2 ratio.

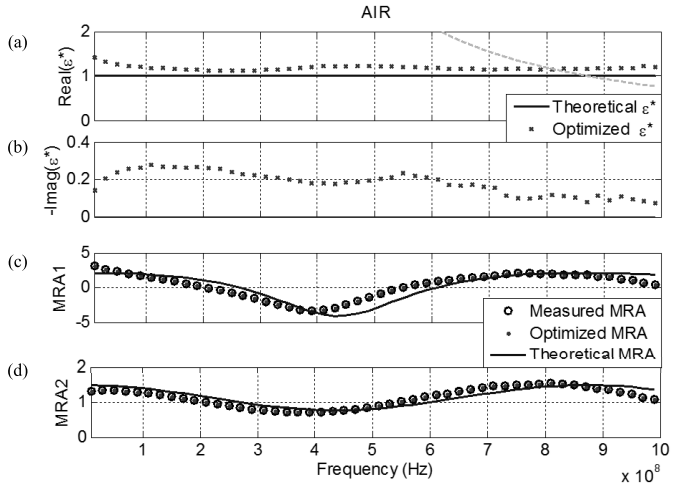

Fig. 21. MRA1 on AIR. (a) Real $\varepsilon^*(f)$. (b) -Imaginary $\varepsilon^*(f)$. (c) MRA1 ratio. (d) MRA2 ratio.

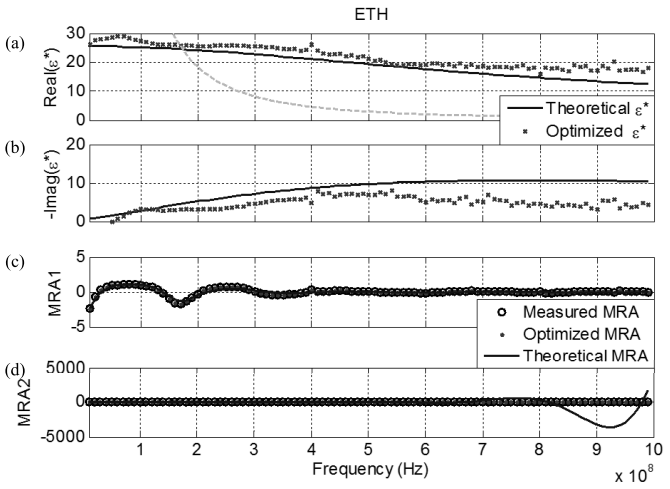

Fig. 23. MRA1 on ETH. (a) Real $\varepsilon^*(f)$. (b) -Imaginary $\varepsilon^*(f)$. (c) MRA1 ratio. (d) MRA2 ratio.

using 5-ps sampling under a controlled room temperature of 24°C(±0.4°C).

The self-developed coaxial field probe for water quality monitoring was manufactured from stainless steel into a 100-mm modularized 50-Ω matched probe head and a 170-mm coaxial sensing section. The probe sensing section consists of an internal conductor rod and a cylindrical external conductor casing. The configuration and cross section geometry of the matched coaxial probe are shown in Fig. 16. The probe head is impedance matched to the coaxial cable to avoid unwanted reflections between the first main reflection and remaining multiple reflections within the sensing section. The modularized field probe allowed the faulty components to be replaced easily in case of damage and ensured that the open-ended internal conductor is fixed to center. The probe casing was perforated at equal intervals to allow the MUT to flow into the sensing region when immersed. The probe was connected to a 42-m long $50-\Omega$ coaxial cable to simulate field deployment. Although the incident step pulse has a bandwidth of 3.35 GHz, high-frequency components beyond 1 GHz were mostly filtered out by the long cable of the field probe. All MUTs were measured with time window duration of 2×10^{-7} s, resulting in lowest measurable frequency of 5 MHz. This data acquisition setup is sufficient to provide a measurement range from 10 MHz to 1 GHz. In fact, many other TDR devices with lower bandwidth, such as those routinely used in soil moisture monitoring, can be used as long as they have a bandwidth greater than the maximum frequency of interest.

Measured experimental TDR signals of all selected MUTs are shown in Fig. 17, where less dispersive MUT is shown in Fig. 17(a), while dispersive alcohols are shown in Fig. 17(b). The time-domain signals were truncated from 1 m before probe head and were aligned at zero point for presentation clarity. Ambient noise levels were suppressed by stacking 12 measurement signals for each MUT. By initial inspection, experimental waveforms matched closely to simulated waveforms but with some added noise. The steady-state level of

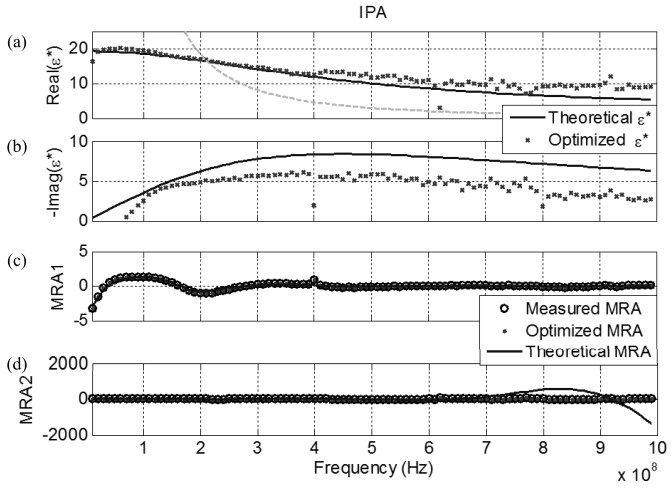

Fig. 24. MRA1 on IPA. (a) Real $\varepsilon^*(f)$. (b) -Imaginary $\varepsilon^*(f)$. (c) MRA1 ratio. (d) MRA2 ratio.

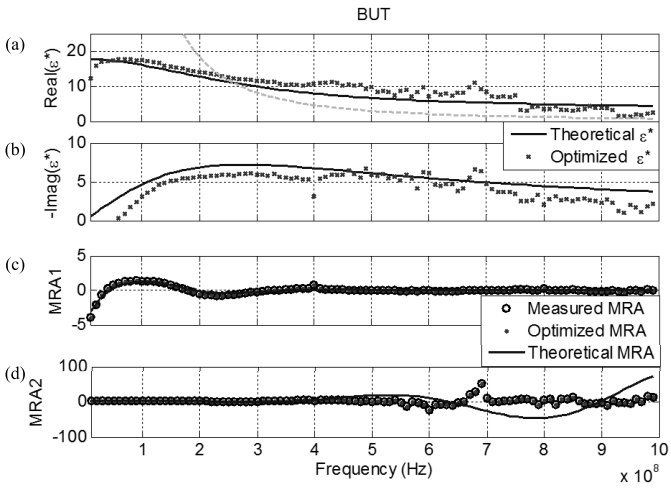

Fig. 25. MRA1 on BUT. (a) Real $\varepsilon^*(f)$. (b) -Imaginary $\varepsilon^*(f)$. (c) MRA1 ratio. (d) MRA2 ratio.

some MUT was not exactly the same as simulated signals due to the consistency of input scaling of the broadband TDR reflectometer, which, however, do not affect the MRA measurement, another advantage of MRA method.

In order to measure accurate CDP spectrum, MRA requires accurately determined probe length (L) and the impedance ratio of probe head and probe sensing section ($Z_{\rm ch}/Z_{p1}$). Since manual measurement of probe length may not be precise and insufficient for short probes, probe length calibration is preferably conducted by measuring a material with well-established CDP spectrum, such as DIS. $Z_{\rm ch}/Z_{p1}$ ratio can either be measured from EM theory for regular geometric cross section probes using (20),or easily calibrated by using the same calibration material in probe length calibration for irregular probes. System parameters of the sensing probe adopted in this paper was calibrated to be: 1) probe length = 171.60 mm and 2) $Z_{\rm ch}/Z_{p1} = 0.5155$.

B. Performance of MRA Method on Experimental Signals

Experimental signals of the eight MUTs were processed with MRA1 procedure in the frequency range from 10 MHz to 1 GHz. CDP spectrum frequency interval was set as 5 MHz during optimization and later downsampled to 15 MHz for presentation clarity. Due to the presence of ambient noise in the experimental signals, appropriate filter was applied to the differentiated time-domain signals prior to MRA procedures for higher signal-to-noise ratio. MRA optimization process on experimental signals was performed using the iterated initial guess method to create an initial-guess-independent optimization environment. $\varepsilon^*_{{\rm ini},f(1)} = 10+i$ was selected as the initial guess for each MUT. MRA generated CDP spectrums from experimental signals of each MUT are shown in Figs 18–25, with subplots (a), (b), (c), and (d) being the real part and imaginary part of CDP, MRA1 ratio, and MRA2 ratio, respectively. Theoretical values are plotted as solid lines, while measured values are plotted as markers, and the corresponding lower frequency limit is plotted in subplot (a) according to (22).

Compared to numerical CDP spectrums, the value oscillations in experimental CDP spectrums were all relatively significant due to the presence of the ambient noise. Measured CDP error within the reliable frequency range is within 5% percentage error margin for all MUTs and around 20% percentage error for dispersive materials beyond certain higher frequency. ACE and AIR have the lowest dielectric dispersion and electrical conductivity effect in the TDR frequency range (10 MHz to 1 GHz), hence their CDP spectrums are relatively stable and nonoscillating, as shown in Figs. 20 and 21. Consistency of CDP spectrum at higher frequencies for DIS and TAP were slightly reduced than the simulated data, which may be caused by ambient noise and physical frequency filtering effect due to the precedent long coaxial cable, leading to the loss of high-frequency information. As for all four alcohol type MUTs, their dielectric dispersion effect and their dielectric drop within TDR frequency range is higher than the other four MUT. The dispersive R_1 signal of alcohols caused some leakage into the extracted $R_{\rm remaining}$ and signal truncation in the noisy differentiated signal would further affect the accuracy of CDP spectrum above 600 MHz. Oscillation error maybe further mitigated by increasing the signal-to-noise ratio of the experimental signals, either by additional waveform stacking, noise filtering or conducting measurement with a shorter leading cable in a lower ambient noise environment.

Observing all optimized and measured MRA spectral ratios of the experimental signals, the application of iterated initial guess in MRA is once again proven to solve the multiple local minimum issue in optimization process. This omits the necessity to have prior information regarding the possible dielectric permittivity range of the MUT and provides a model-free approach in CDP measurement. Upper frequency limit of CDP spectrum can be easily identified either by direct inspection, or by crosschecking both the trend of MRA1 and MRA2 ratios. The measured MRA2 ratios of dispersive materials at higher frequencies deviate significantly from the theoretical values. This can be used to identify the upper frequency limit of dispersive MUT.

V. Conclusion

This paper proposed a rapid, robust, and model-free MRA of TDR signal to measure the complete CDP spectrum within the TDR frequency range of 10 MHz to 1 GHz. The key to this innovative approach is to decompose the TDR signal into the first top reflection and the remaining all multiple reflections. The spectral ratio of these two parts (MRA ratio) was theoretically derived as a function of CDP, independent of source function and condition in the leading transmission line sections. Based on this theoretical formulation, CDP spectrum can be uniquely inverted from the measured MRA ratio. An insightful iterated initial guess approach was implemented during CDP inversion, which used the unique inverted CDP value of the well-posed problem at the lowest frequency as the initial guess for the next higher frequency step, hence preventing the inversion optimization from falling into a local minimum at higher frequencies.

The performance of MRA was evaluated and validated using both synthetic and experimental TDR signals of eight MUTs, covering both nondispersive and dispersive materials from high to low dielectric permittivity. Both numerical and experimental results agreed well, but higher oscillation error was found in experimental results due to ambient noise and truncation and leakage associated with the long cable used. Straightforward MRA signal processing algorithm enables dielectric spectroscopy to be conveniently conducted in laboratory and field, without complicated system setup and calibration. This may allow *in situ* CDP spectrum monitoring to be performed reliably and economically, which may possibly be a breakthrough in the dielectric spectroscopy field. Conventional TDR measurements based on single-valued travel time and apparent dielectric constant may benefit from this proposed method, by revealing the CDP spectrum through the same set of time-domain signals and providing further insights into frequency-dependent physical parameters. Future studies in developing a measurement system with steady, nonleaking R_1 signal is recommended to further improve the CDP measurement.

References

[1] U. Kaatze, "Measuring the dielectric properties of materials. Ninety-year development from low-frequency techniques to broadband spectroscopy and high-frequency imaging," *Meas. Sci. Technol.*, vol. 24, no. 1, p. 012005, 2013.

[2] F. Kremer and A. Schönhals, *Broadband Dielectric Spectroscopy*. Berlin, Germany: Springer, 2003.

[3] J. Y. Fu, "On the theory of the universal dielectric relaxation," *Philos. Mag.*, vol. 94, no. 16, pp. 1788–1815, Jun. 2014.

[4] J. C. Santamarina, K. A. Klein, and M. A. Fam, *Soils and Waves*. Hoboken, NJ, USA: Wiley, 2001.

[5] F. X. Hassion and R. H. Cole, "Dielectric properties of liquid ethanol and 2-propanol," *J. Chem. Phys.*, vol. 23, no. 10, pp. 1756–1761, Oct. 1955.

[6] T. Sato and R. Buchner, "Dielectric relaxation spectroscopy of 2-propanol-water mixtures," *J. Chem. Phys.*, vol. 118, no. 10, pp. 4606–4613, 2003.

[7] M. Mohsen-Nia, H. Amiri, and B. Jazi, "Dielectric constants of water, methanol, ethanol, butanol and acetone: Measurement and computational study," *J. Solution Chem.*, vol. 39, no. 5, pp. 701–708, May 2010.

[8] P. Sivagurunathan, K. Dharmalingam, K. Ramachandran, B. P. Undre, P. W. Khirade, and S. C. Mehrotra, "Dielectric studies on binary mixtures of ester with alcohol using time domain reflectometry," *J. Mol. Liquids*, vol. 133, nos. 1–3, pp. 139–145, 2007.

[9] Z. J. Sun, G. D. Young, R. A. McFarlane, and B. M. Chambers, "The effect of soil electrical conductivity on moisture determination using time-domain reflectometry in sandy soil," *Can. J. Soil Sci.*, vol. 80, no. 1, pp. 13–22, 2000.

[10] M. C. Dobson, F. T. Ulaby, M. T. Hallikainen, and M. A. El-rayes, "Microwave dielectric behavior of wet soil-part II: Dielectric mixing models," *IEEE Trans. Geosci. Remote Sens.*, vol. GE-23, no. 1, pp. 35–46, Jan. 1985.

[11] T. J. Heimovaara, "Frequency domain analysis of time domain reflectometry waveforms: 1. Measurement of the complex dielectric permittivity of soils," *Water Resour. Res.*, vol. 30, no. 2, pp. 189–199, Feb. 1994.

[12] G. C. Topp, S. Zegelin, and I. White, "Impacts of the real and imaginary components of relative permittivity on time domain reflectometry measurements in soils," *Soil Sci. Soc. Amer. J.*, vol. 64, no. 4, p. 1244, 2000.

[13] C.-P. Lin, "Frequency domain versus travel time analyses of TDR waveforms for soil moisture measurements," *Soil Sci. Soc. Amer. J.*, vol. 67, no. 3, pp. 720–729, 2003.

[14] R. Friel and D. Or, "Frequency analysis of time-domain reflectometry (TDR) with application to dielectric spectroscopy of soil constituents," *Geophysics*, vol. 64, no. 3, pp. 707–718, May 1999.

[15] C. J. F. Bottcher and P. Bordewijk, *Theory of Electric Polarization*, vol. 1, 2nd ed. Amsterdam, The Netherlands: Elsevier, 1978.

[16] F. Grasso, F. Musumeci, and A. Triglia, "Impedance spectroscopy of pure water in the 0.01 Hz to 100 kHz range," *Il Nuovo Cimento D*, vol. 12, no. 8, pp. 1117–1130, Aug. 1990.

[17] E. Barsoukov and J. R. Macdonald, *Impedance Spectroscopy*. Hoboken, NJ, USA: Wiley, 2005. [Online]. Available: http://doi.wiley.com/10.1002/0471716243

[18] K. Zonge, J. Wynn, and S. Urquhart, "9. Resistivity, induced polarization, and complex resistivity," in *Near-Surface Geophysics*. Tulsa, Oklahoma: Society of Exploration Geophysicists, 2005, pp. 265–300.

[19] E. Zimmermann, A. Kemna, J. Berwix, W. Glaas, H. M. Münch, and J. A. Huisman, "A high-accuracy impedance spectrometer for measuring sediments with low polarizability," *Meas. Sci. Technol.*, vol. 19, no. 10, p. 105603, 2008.

[20] P. J. Koelemeijer, C. J. Peach, and C. J. Spiers, "Surface diffusivity of cleaved NaCl crystals as a function of humidity: Impedance spectroscopy measurements and implications for crack healing in rock salt," *J. Geophys. Res. Solid Earth*, vol. 117, no. B1, p. B01205, 2012. [Online]. Available: https://agupubs.onlinelibrary.wiley.com/doi/abs/10.1029/2011JB008627

[21] A. Revil, "Effective conductivity and permittivity of unsaturated porous materials in the frequency range 1 mHz–1GHz," *Water Resour. Res.*, vol. 49, no. 1, pp. 306–327, 2013.

[22] A. Szypłowska, A. Nakonieczna, A. Wilczek, B. Paszkowski, G. Solecki, and W. Skierucha, "Application of a coaxial-like sensor for impedance spectroscopy measurements of selected low-conductivity liquids," *Sensors*, vol. 13, no. 10, pp. 13301–13317, Sep. 2013.

[23] S. D. Logsdon, "Soil dielectric spectra from vector network analyzer data," *Soil Sci. Soc. Amer. J.*, vol. 69, pp. 983–989, 2005.

[24] A. Cataldo, L. Catarinucci, L. Tarricone, F. Attivissimo, and E. Piuzzi, "A combined TD–FD method for enhanced reflectometry measurements in liquid quality monitoring," *IEEE Trans. Instrum. Meas.*, vol. 58, no. 10, pp. 3534–3543, Oct. 2009.

[25] N. Wagner, K. Emmerich, F. Bonitz, and K. Kupfer, "Experimental investigations on the frequency- and temperature-dependent dielectric material properties of soil," *IEEE Trans. Geosci. Remote Sens.*, vol. 49, no. 7, pp. 2518–2530, Jul. 2011.

[26] N. Wagner, M. Schwing, and A. Scheuermann, "Numerical 3-D FEM and experimental analysis of the open-ended coaxial line technique for microwave dielectric spectroscopy on soil," *IEEE Trans. Geosci. Remote Sens.*, vol. 52, no. 2, pp. 880–893, Feb. 2014.

[27] M. Schwing, N. Wagner, J. Karlovsek, Z. Chen, D. J. Williams, and A. Scheuermann, "Radio to microwave dielectric characterisation of constitutive electromagnetic soil properties using vector network analyses," *J. Geophys. Eng.*, vol. 13, no. 2, p. S28, 2016.

[28] T. Bore, M. H. Bhuyan, T. Bittner, V. Murgan, N. Wagner, and A. Scheuermann, "A large coaxial reflection cell for broadband dielectric characterization of coarse-grained materials," *Meas. Sci. Technol.*, vol. 29, no. 1, p. 015602, Oct. 2017.

[29] J. Minet, S. Lambot, G. Delaide, J. A. Huisman, H. Vereecken, and M. Vanclooster, "A generalized frequency domain reflectometry modeling technique for soil electrical properties determination," *Vadose Zone J.*, vol. 9, no. 4, pp. 1063–1072, 2010.

[30] W. Skierucha and A. Wilczek, "A FDR sensor for measuring complex soil dielectric permittivity in the 10–500 MHz frequency range," *Sensors*, vol. 10, no. 4, pp. 3314–3329, 2010.

[31] N. E. Hager, "Broadband time-domain-reflectometry dielectric spectroscopy using variable-time-scale sampling," *Rev. Sci. Instrum.*, vol. 65, no. 4, pp. 887–891, 1994.

[32] A. H. Weerts, J. A. Huisman, and W. Bouten, "Information content of time domain reflectometry waveforms," *Water Resour. Res.*, vol. 37, no. 5, pp. 1291–1299, 2001.

[33] A. Cataldo and E. De Benedetto, "Broadband reflectometry for diagnostics and monitoring applications," *IEEE Sensors J.*, vol. 11, no. 2, pp. 451–459, Feb. 2011.

[34] C.-P. Lin, Y. J. Ngui, and C.-H. Lin, "A novel TDR signal processing technique for measuring apparent dielectric spectrum," *Meas. Sci. Technol.*, vol. 28, no. 1, p. 015501, 2017.

[35] S. B. Jones and D. Or, "Frequency domain analysis for extending time domain reflectometry water content measurement in highly saline soils," *Soil Sci. Soc. Amer. J.*, vol. 68, no. 5, pp. 1568–1577, 2004.

[36] J. M. Wraith and D. Or, "Temperature effects on soil bulk dielectric permittivity measured by time domain reflectometry: Experimental evidence and hypothesis development," *Water Resour. Res.*, vol. 35, no. 2, pp. 361–369, 1999.

[37] R. C. Schwartz, S. R. Evett, M. G. Pelletier, and J. M. Bell, "Complex permittivity model for time domain reflectometry soil water content sensing: I. Theory," *Soil Sci. Soc. Amer. J.*, vol. 73, no. 3, pp. 886–897, 2009.

[38] M. Persson and R. Berndtsson, "Measuring nonaqueous phase liquid saturation in soil using time domain reflectometry," *Water Resour. Res.*, vol. 38, no. 5, pp. 22-1–22-8, 2002.

[39] A. Comegna, A. Coppola, G. Dragonetti, and A. Sommella, "Dielectric response of a variable saturated soil contaminated by non-aqueous phase liquids (NAPLs)," *Procedia Environ. Sci.*, vol. 19, pp. 701–710, Jan. 2013.

[40] C.-P. Lin, S.-H. Tang, W.-C. Lin, and C.-C. Chung, "Quantification of cable deformation with time domain reflectometry-implications to landslide monitoring," *J. Geotech. Geoenvironment. Eng.*, vol. 135, pp. 143–152, Jan. 2009.

[41] C.-H. Lin, C.-P. Lin, and V. Drnevich, "TDR method for compaction quality control: Multi evaluation and sources of error," *Geotech. Test. J.*, vol. 35, no. 5, pp. 1–10, Sep. 2012.

[42] C.-C. Chung, C.-P. Lin, K. Wang, C.-S. Lin, and Y. J. Ngui, "Improved TDR method for quality control of soil-nailing works," *J. Geotech. Geoenvironment. Eng.*, vol. 142, no. 1, p. 06015011, 2016.

[43] C. Dowding, J. A. Summers, A. Taflove, and W. L. Kath, "Electromagnetic wave propagation model for differentiation of geotechnical disturbances along buried cables," *Geotech. Test. J.*, vol. 25, no. 4, pp. 449–458, 2002.

[44] H. Bhuyan, A. Scheuermann, D. Bodin, and R. Becker, "Use of time domain reflectometry to estimate moisture and density of unbound road materials," *Transp. Res. Rec. J. Transp. Res. Board*, vol. 2655, pp. 71–81, Jan. 2017. [Online]. Available: http://dx.doi.org/10.3141/2655-10

[45] N. E. Hager and R. C. Domszy, "Monitoring of cement hydration by broadband time-domain-reflectometry dielectric spectroscopy," *J. Appl. Phys.*, vol. 96, no. 9, p. 5117, 2004.

[46] C.-C. Chung and C.-P. Lin, "High concentration suspended sediment measurements using time domain reflectometry," *J. Hydrol.*, vol. 401, nos. 1–2, pp. 134–144, 2011.

[47] J. Ledieu, P. De Ridder, P. De Clerck, and S. Dautrebande, "A method of measuring soil moisture by time-domain reflectometry," *J. Hydrol.*, vol. 88, nos. 3–4, pp. 319–328, Nov. 1986.

[48] C. Dirksen and S. Dasberg, "Improved calibration of time domain reflectometry soil water content measurements," *Soil Sci. Soc. Amer. J.*, vol. 57, no. 3, p. 660, 1993.

[49] M. Yanuka, G. C. Topp, S. Zegelin, and W. D. Zebchuk, "Multiple reflection and attenuation of time domain reflectometry pulses: Theoretical considerations for applications to soil and water," *Water Resour. Res.*, vol. 24, no. 7, pp. 939–944, Jul. 1988.

[50] W. Feng, C. P. Lin, R. J. Deschamps, and V. P. Drnevich, "Theoretical model of a multisection time domain reflectometry measurement system," *Water Resour. Res.*, vol. 35, no. 8, p. 2321, 1999.

[51] C.-P. Lin and S.-H. Tang, "Comprehensive wave propagation model to improve TDR interpretations for geotechnical applications," *Geotech. Test. J.*, vol. 30, no. 2, pp. 90–97, 2007.

[52] K. Giese and R. Tiemann, "Determination of the complex permittivity from thin-sample time domain reflectometry improved analysis of the step response waveform," *Adv. Mol. Relaxation Process.*, vol. 7, no. 1, pp. 45–59, May 1975.

[53] T. S. Clarkson, L. Glasser, R. W. Tuxworth, and G. Williams, "An appreciation of experimental factors in time-domain spectroscopy," *Adv. Mol. Relaxation Interact. Process.*, vol. 10, no. 3, pp. 173–202, Jul. 1977.

[54] E. Piuzzi, A. Cataldo, G. Cannazza, and E. De Benedetto, "An improved reflectometric method for soil moisture measurement exploiting an innovative triple-short calibration," *IEEE Trans. Instrum. Meas.*, vol. 59, no. 10, pp. 2747–2754, Oct. 2010.

[55] C.-P. Lin, S.-H. Tang, C.-H. Lin, and C.-C. Chung, "An improved modeling of TDR signal propagation for measuring complex dielectric permittivity," *J. Earth Sci.*, vol. 26, no. 6, pp. 827–834, 2015.

[56] A. Szyplowska, A. Wilczek, M. Kafarski, and W. Skierucha, "Soil complex dielectric permittivity spectra determination using electrical signal reflections in probes of various lengths," *Vadose Zone J.*, vol. 15, no. 3, 2016.

[57] J. W. Tukey, "An introduction to the calculations of numerical spectrum analysis," *Spectr. Anal. Time Ser.*, pp. 25–46, 1967.

[58] M. Frigo and S. G. Johnson, "FFTW: An adaptive software architecture for the FFT," in *Proc. IEEE Int. Conf. Acoust., Speech Signal Process.*, vol. 3. May 1998, pp. 1381–1384.

[59] K. S. Cole and R. H. Cole, "Dispersion and absorption in dielectrics I. Alternating current characteristics," *J. Chem. Phys.*, vol. 9, no. 4, p. 341, 1941.

[60] W. C. Elmore and M. A. Heald, *Physics of Waves*. New York, NY, USA: Dover, 1985.

[61] J. B. Hasted, *Aqueous Dielectric*. New York, NY, USA: Chapman & Hall, 1973.

[62] *MATLAB 2013a*. The MathWorks Inc., Natick, MA, USA, 2013.

Chih-Ping Lin received the Master of Science degree in civil engineering, the Master of Science degree in electrical and computer engineering, and the Ph.D. degree from Purdue University, West Lafayette, IN, USA, in 1996, 1998, and 1999, respectively.

Since 1999, he has been a Faculty Member with the National Chiao Tung University, Hsinchu, Taiwan, where he is currently a Professor and the Chair with the Department of Civil Engineering. His current research interests include engineering monitoring based on electromagnetic time-domain reflectometry (TDR), and developments and applications of near-surface geophysics for solving engineering problems. The TDR-based measurements being developed ranges from soil moisture, suspended sediment concentration, water level, extensometer, localized shear deformation, scouring, and to dielectric spectroscopy.

Dr. Lin was a recipient of the ASTM Hogentogler Award in 2008. He served on the board of the Environmental and Engineering Geophysical Society from 2010 to 2013.

Yin Jeh Ngui received the B.Eng. degree (Hons) in civil engineering from the Hong Kong Polytechnic University, Hong Kong, in 2013. He is currently pursuing the Ph.D. degree in civil engineering with National Chiao Tung University, Hsinchu, Taiwan, with a focus on geotechnical engineering.

His current research interests include broadband dielectric spectroscopy involving time-domain reflectometry, dielectric measurements in contaminated sites, and electrical resistivity tomography.

Dr. Ngui was a recipient of three Best Student Paper Award in 2013 for his undergraduate final year project from the Chartered Institution of Highways and Transportation, ASCE Hong Kong Section, and Institute of Civil Engineers Hong Kong Association.

Chun-Hung Lin received the Ph.D. degree in geotechnical engineering from National Chiao Tung University, Hsinchu, Taiwan, in 2012.

He is currently an Assistant Professor with the Department of Marine Environment and Engineering, National Sun Yat-Sen University, Kaohsiung, Taiwan. His current research interests include the applications of engineering geophysics in marine engineering, engineering monitoring based on geophysics and time-domain reflectometry, and development of sensors.